


Article

Hydrothermal and Co-Precipitation Combined with Photo-Reduced Preparation of Ag/AgBr/MgBi₂O₆ Composites for Visible Light Degradation Toward Organics

Hsin-Yi Huang ¹, Mudakazhi Kanakkithodi Arun ^{1,2,3}, Sabu Thomas ², Mei-Yao Wu ⁴, Tsunghsueh Wu ⁵ and Yang-Wei Lin ^{1,*} 

¹ Department of Chemistry, National Changhua University of Education, 1 Jin-De Road, Changhua City 50007, Taiwan; m0925011@gm.ncue.edu.tw (H.-Y.H.); arunbaburaj99@gmail.com (M.K.A.)

² School of Nano Science and Nano Technology, Mahatma Gandhi University, Priyadarshini Hills P. O., Kottayam 686560, India; sabuthomas@mgu.ac.in

³ Department of Physics, Kannur University, Swami Anandatheertha Campus, Payyanur Edat P. O., Kannur 670327, India

⁴ School of Post-Baccalaureate Chinese Medicine, China Medical University, 91, Hsueh-Shih Road, Taichung 40424, Taiwan; meiyawu@mail.cmu.edu.tw

⁵ Department of Chemistry, University of Wisconsin-Platteville, 1 University Plaza, Platteville, WI 53818, USA; wut@uwplatt.edu

* Correspondence: linywjerry@cc.ncue.edu.tw; Tel.: +886-4-7232105-3553

Abstract: This study developed a MgBi₂O₆-based photocatalyst via low-temperature hydrothermal synthesis. AgBr was co-precipitated onto MgBi₂O₆, and silver nanoparticles (AgNPs) were photo-reduced onto the surface. The photocatalytic performance, assessed by methylene blue (MB) degradation under white-light LED irradiation (2.5 W, power density = 0.38 W/cm²), showed that Ag/AgBr/MgBi₂O₆ achieved 98.6% degradation in 40 min, outperforming MgBi₂O₆ (37.5%) and AgBr/MgBi₂O₆ (85.5%). AgNPs boosted electron-hole separation via surface plasmon resonance, reducing recombination. A Z-scheme photocatalytic mechanism was suggested, where photogenerated carriers transferred across the p–n heterojunction between AgBr and MgBi₂O₆, producing reactive oxygen species like superoxide and hydroxyl radicals critical for dye degradation. Thus, the Ag/AgBr/MgBi₂O₆ composites possessed excellent photocatalytic performance regarding dyestuff degradation (85.8–99.9% degradation within 40 min) under white-light LED irradiation.

Keywords: photoreduction; AgNPs; AgBr; MgBi₂O₆; methylene blue; Z-scheme mechanism



Citation: Huang, H.-Y.; Arun, M.K.; Thomas, S.; Wu, M.-Y.; Wu, T.; Lin, Y.-W. Hydrothermal and Co-Precipitation Combined with Photo-Reduced Preparation of Ag/AgBr/MgBi₂O₆ Composites for Visible Light Degradation Toward Organics. *Nanomaterials* **2024**, *14*, 1865. <https://doi.org/10.3390/nano14231865>

Academic Editor: Diego Cazorla-Amorós

Received: 4 November 2024

Revised: 16 November 2024

Accepted: 20 November 2024

Published: 21 November 2024



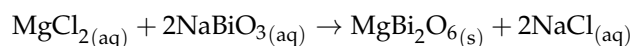
Copyright: © 2024 by the authors. Licensee MDPI, Basel, Switzerland. This article is an open access article distributed under the terms and conditions of the Creative Commons Attribution (CC BY) license (<https://creativecommons.org/licenses/by/4.0/>).

1. Introduction

With increased industrialization, significant volumes of organic contaminants, including dyes and waste oils, are discharged into the environment, posing serious threats to biodiversity, human health, and ecosystems [1,2]. Traditional chemical industries contribute heavily to this pollution. Conventional methods for treating contaminants, emerging contaminants of concern (CECs), and wastewater effluents include activated sludge biological systems, activated carbon adsorption, membrane filtration, and chemical treatments. These treatments can be broadly categorized into traditional methods, such as chlorination and biological processes, and advanced oxidation processes (AOPs), including ozonation, ultraviolet irradiation, and potassium permanganate oxidation. AOPs are particularly effective in addressing complex pollutants that are resistant to conventional methods [3–5]. To address the diverse advantages and disadvantages of the previously mentioned treatments, greener alternatives such as electrochemical catalysis, semiconductor photocatalysis, Fenton reactions, and supercritical water oxidation have been developed [6–11]. These methods aim to overcome specific limitations while offering tailored benefits depending

on the nature of the contaminants and treatment goals. However, electrochemical catalysis and supercritical water oxidation face energy and cost limitations, and Fenton-based methods risk secondary pollution from iron sludge [12,13]. In contrast, semiconductor photocatalysis is a renewable and continuous process, offering a promising approach to addressing environmental pollution and energy shortages [14,15].

Bi(III)-based compounds have recently gained attention as photocatalytic materials due to their unique electronic structures. Bismuth compounds and their derivatives are non-toxic and biologically inert, leading to diverse applications [16,17]. Numerous photocatalysts have been synthesized from these compounds, including Bi_2S_3 , Bi_2WO_6 , and $\text{Bi}_2\text{Ti}_2\text{O}_7$ [10,18,19]. Bismuth sulfide and bismuth oxide have energy gaps below 2.0 eV, allowing them to absorb light in the visible spectrum [20,21]. This study focuses on the potential of MgBi_2O_6 , a noteworthy compound synthesized as an oxide of Bi(V) with a distinctive mirror triple-rutile crystal structure. Unlike Bi(III), where electrons occupy the 6s orbital, Bi(V) in MgBi_2O_6 features unfilled 6s orbitals, allowing greater flexibility in electron arrangements and enhanced photocatalytic potential. Although research on magnesium bismuthate is limited, MgBi_2O_6 shows promise as a significant contributor to the field of photocatalysis. Its synthesis involves a substitution reaction between magnesium chloride and sodium bismuthate, as follows:



with an energy gap of approximately 1.8 eV, MgBi_2O_6 facilitates efficient electronic transitions. Literature indicates that MgBi_2O_6 exhibits strong visible-light absorption and demonstrates significant activity in degrading methylene blue (MB) under visible light [22,23]. Due to these properties, MgBi_2O_6 was selected as the primary photocatalyst in this study, with additional materials incorporated to enhance its degradation performance.

Silver halides (AgX , $X = \text{Cl}$, Br , and I) are susceptible to photo-corrosion in photocatalytic reactions, as Ag(I) is readily reduced to metallic Ag(0) by photogenerated electrons. Silver halides are often anchored to various surfaces to address this limitation, enhancing stability [24,25]. Strategies to mitigate photo-corrosion include coupling silver halides with TiO_2 via heterojunctions or attaching them to magnetic carriers [26]. Additionally, modifications such as using ZnWO_4 for band alignment allow photogenerated electrons from AgBr to transfer effectively to ZnWO_4 , thus enhancing stability [27]. Another widely applied method is constructing Z-scheme heterojunctions, which are a type of semiconductor heterojunctions that facilitate efficient charge transfer by utilizing the difference in the energy levels of the two semiconductors, significantly boosting photoactivity and stability [28,29]. Among silver halides, AgCl has strong absorption in the UV range, while AgBr has a visible light absorption edge at 475 nm [30–32]. Consequently, this experiment employed AgBr -modified MgBi_2O_6 to enhance visible light absorption.

When exposed to visible light, the conduction electrons on the surface of silver nanoparticles (AgNPs) play a crucial role in photocatalysis. They can oscillate collectively at a resonant frequency, a phenomenon known as surface plasmon resonance (SPR) [32,33]. When the frequency of incoming photons aligns with the natural oscillation frequency of surface electrons, plasmonic metal nanostructures (such as gold, silver, and copper) strongly interact with this light, intensifying local SPR effects [33]. This interaction leads to the enhancement of photocatalytic activity within the visible light spectrum [34,35]. Methods for depositing AgNPs onto photocatalytic materials generally involve AgX reduction, which can occur through chemical reduction, thermal reduction, or light-induced reduction. In this experiment, AgBr served as the precursor, and AgNPs were synthesized via light-induced reduction and deposited on $\text{AgBr}/\text{MgBi}_2\text{O}_6$ surfaces. Studies suggest that in Ag/AgX ($X = \text{Cl}$, Br , I) systems, this combination forms a photocatalyst with a narrow energy gap, effectively enhancing visible light responsiveness [36,37]. The Ag/AgBr photocatalyst shows superior catalytic activity compared to Ag/AgCl , as bromine (Br^0) has a lower electron affinity than chlorine (Cl^0), resulting in a narrower energy gap (approximately

2.6 eV) [38]. This characteristic improves catalytic efficiency and photostability, although rapid electron-hole recombination still presents challenges for broader applications.

With the rapid advancement of science, technology, and industrial activity, wastewater containing various organic pollutants is increasingly released, contributing significantly to environmental pollution. Since the pioneering work by Fujishima and Honda, TiO_2 has become widely used as a photocatalyst due to its stability, diversity, and non-toxicity [39,40]. However, TiO_2 's application is constrained by its reliance on ultraviolet light for activation [41]. Our study employs pentavalent bismuth-based MgBi_2O_6 as a photocatalyst substrate to address this limitation. Although MgBi_2O_6 is not the most active among pentavalent bismuth compounds, its effectiveness in degrading organic pollutants like MB can be enhanced by modifying its surface with AgBr, thereby adjusting the band gap for improved photocatalytic performance. In addition, AgNPs are deposited onto the surface of AgBr/ MgBi_2O_6 via a light-induced reduction method. This process leverages the SPR effect to intensify the local electromagnetic field around the nanoparticles, thereby improving electron-hole separation. Combining AgBr and AgNPs enables enhanced visible light absorption and reduces electron-hole recombination rates. Since SPR is influenced by nanoparticle size, content, and dispersion factors, this study optimizes the light-induced reduction time to control these factors for maximal photodegradation efficiency. Using visible light, the Ag/AgBr/ MgBi_2O_6 photocatalyst degrades the organic dye (MB), with electrochemical analyses measuring charge separation and electron-hole recombination rates. Additionally, scavenger experiments identify key reactive radicals involved in the photodegradation process. Following the reaction, total organic carbon (TOC) analysis confirms the mineralization of organic pollutants. The prepared Ag/AgBr/ MgBi_2O_6 photocatalyst shows promise for future applications in sunlight-driven degradation of actual wastewater samples.

2. Materials and Methods

2.1. Chemicals

All reagents used were obtained from Sigma Aldrich (St. Louis, MO, USA) and were of analytical grade without further purification. Milli-Q ultrapure water was used in all of the experiments.

2.2. Characterization of the Prepared MgBi_2O_6 -Based Composites

An X-ray diffractometer (Model: SMART APEX II, Bruker AXS, Billerica, MA, USA) with Cu $K\alpha$ radiation ($\lambda = 0.15418$ nm) and a scanning electron microscope (SEM) (Model: HITACHI S-4300, Hitachi High Technologies Corporation, Tokyo, Japan) operating at 15 kV and equipped with a QUANTAX Annular XFlash QUAD FQ5060 detector (Bruker Nano, Berlin, Germany) were utilized to determine X-ray diffraction (XRD) patterns and to observe the morphology and composition of MgBi_2O_6 , AgBr/ MgBi_2O_6 , and Ag/AgBr/ MgBi_2O_6 composites. Additionally, X-ray photoelectron spectroscopy (XPS) spectra were obtained using a VG ESCA210 electron spectroscope (VG Scientific, West Sussex, UK). For UV-visible diffuse reflectance (UV-Vis DRS) spectra, a UV-visible spectrometer (Model: Evolution 2000, Thermo Fisher Scientific Inc., Madison, WI, USA) with a BaSO_4 reference was used.

2.3. Synthesis of Ag/AgBr/ MgBi_2O_6 Composites

Detailed synthesis procedures for MgBi_2O_6 and AgBr/ MgBi_2O_6 are provided in the Supplementary Information. To synthesize the Ag/AgBr/ MgBi_2O_6 composite, weigh 0.5383 g of AgBr/ MgBi_2O_6 and add it to 30 mL of deionized water to prepare solution A. Stir solution A in a dark room at 600 rpm for 15 min. Weigh 0.5383 g of AgNO_3 , corresponding to the weight ratio of AgNO_3 to AgBr/ MgBi_2O_6 of 1:1. Dissolve each amount of AgNO_3 in 30 mL of deionized water to prepare solution B. Add solution B dropwise to the stirring solution A while illuminating with a 300 W mercury-xenon lamp. Stir the mixture at 600 rpm for 2 h. Allow the mixture to precipitate in a dry and cool place. Wash the precipitated composite three times with deionized water and once with ethanol,

followed by centrifugation at 12,000 rpm for 10 min using a high-speed centrifuge after each wash. Transfer the final product into a crucible, cover it with aluminum foil, and dry it in an oven at 60 °C to obtain the Ag/AgBr/MgBi₂O₆ composite. Thus, the preparation procedure for the Ag/AgBr/MgBi₂O₆ composites in this study was summarized as follows: In a hydrothermal reactor, the synthesis involves a substitution reaction between magnesium chloride and sodium bismuthate to produce MgBi₂O₆. AgBr is primarily formed through a co-precipitation reaction between AgNO₃ and NaBr. Finally, a mercury-xenon lamp is used to irradiate AgNO₃, facilitating a photo-reduction process that enables silver particles to adhere to the surface of the AgBr/MgBi₂O₆ composite.

2.4. Photodegradation MB Procedure

MgBi₂O₆, AgBr/MgBi₂O₆, and Ag/AgBr/MgBi₂O₆ composites were tested for MB degradation under low-power white-light LED irradiation. MB was selected as the model molecule due to the following: (a) Common pollutant: MB is a widely used industrial dye and a significant environmental pollutant; (b) Ease of monitoring: Its strong absorption peak at ~665 nm allows easy concentration tracking via UV-Vis spectroscopy; (c) Standard for organic pollutants: MB represents the behavior of many dyes, offering insights into photocatalyst efficiency; (d) Well-documented properties: MB's known degradation pathways simplify performance evaluation; and (e) Benchmark material: It is commonly used in photocatalytic studies, enabling comparisons with existing research.

An amount of 150 mg of MgBi₂O₆, AgBr/MgBi₂O₆, or Ag/AgBr/MgBi₂O₆ was added to an aqueous MB solution (15 ppm) in a 50 mL quartz flask maintained at 25 °C. Before irradiation, the mixture was stirred in the dark for 30 min to establish adsorption-desorption equilibrium. The suspension was then illuminated with white-light LED lamps (2.5 W, power density = 0.38 W/cm²) using a PCX-50C photoreactor (Beijing Perfectlight Technology Co., Ltd., Beijing, China). At set intervals, 1 mL of the suspension was sampled and centrifuged to remove particulate matter. The concentration of MB was measured using a Synergy H1 hybrid multimode microplate reader (Biotek Instruments, Inc., Winooski, VT, USA) at the characteristic absorption wavelength of 665 nm. Total organic carbon (TOC) was measured during degradation using a TOC analyzer (Elementar Acquray, Elementar Analysensysteme GmbH, Langenselbold, Germany). Similar processes were performed for various dyestuffs (methyl red (MR), methyl orange (MO), rhodamine B (RhB), and rhodamine 6G (R6G)).

2.5. Evaluation of Charge Separation Efficiency and Recombination Rate

The charge separation efficiency and electron-hole recombination rate of the synthesized composites were assessed following established protocols. Electrochemical impedance spectroscopy (EIS) was performed to measure the charge separation efficiency on the surface of MgBi₂O₆, AgBr/MgBi₂O₆, and Ag/AgBr/MgBi₂O₆ composites after 15 min of white-light LED exposure. A slurry, prepared by mixing 0.1 g of the composite with 1.0 mL of ethanol, was applied onto an indium tin oxide (ITO, 9.42 wt% SnO₂ and 89.75 wt% In₂O₃) substrate (resistivity ~10⁻⁴ Ω·cm) and then heated at 50 °C for 30 min to ensure complete ethanol evaporation. The coated ITO glass was subsequently annealed at 200 °C for 2 h to stabilize the composite layer and prevent peeling during testing. This prepared sample was analyzed under white-light LED irradiation using a CHI-6122E electrochemical analyzer (CH Instruments Inc., Austin, TX, USA). The electrochemical setup consists of an Ag/AgCl electrode as the reference, a platinum electrode as the auxiliary, and an electrolyte solution composed of 0.1 M KCl and 5.0 mM K₃[Fe(CN)₆]. The EIS measurement parameters were configured as follows: applied potential of 1.5 V, amplitude of 0.7 V, high frequency of 1.5 × 10⁵ Hz, and low frequency of 0.03831 Hz. Additionally, the electron-hole recombination rate was determined by capturing luminescence spectra with a photoluminescence (PL) spectrometer (Varian Cary Eclipse, Agilent Technologies, Inc., Santa Clara, CA, USA).

2.6. Scavenger Test

To identify the active species involved in the photocatalytic degradation of MB over Ag/AgBr/MgBi₂O₆, trapping experiments were performed using ethylenediaminetetraacetic acid disodium salt (EDTA disodium salt) and tert-butanol (t-BuOH) at 1 mmol as scavengers for holes, and hydroxyl radicals, respectively. The experimental setup followed the standard photocatalytic degradation procedure, with a different scavenger added for each test to inhibit the target reactive species selectively. Additionally, MB degradation in an Ag/AgBr/MgBi₂O₆ system under nitrogen (N₂) atmospheres was analyzed to further confirm the role of oxygen radicals as primary reactive species in the degradation pathway.

3. Results and Discussion

3.1. Characterization

The XRD patterns of MgBi₂O₆, AgBr/MgBi₂O₆, Ag/AgBr/MgBi₂O₆, and AgBr are presented in Figure 1. The MgBi₂O₆ exhibits a mirror-like triple rutile structure, with primary scattering angles at 2θ values of 18.2°, 20.5°, 26.1°, 32.0°, 33.3°, 37.2°, 50.8°, 53.7°, and 64.6°, corresponding to the crystal planes (002), (101), (110), (112), (103), (200), (213), (220), and (303), respectively, in agreement with the JCPDS No. 86-2492 database [42–44]. The cubic AgBr structure aligns with JCPDS No. 79-0149, with main scattering angles at 2θ values of 26.7°, 30.9°, 44.3°, 55.0°, 64.5°, and 73.2°, associated with the crystal planes (111), (200), (220), (222), (400), and (420), respectively [45,46]. The figure shows that the synthesized AgBr/MgBi₂O₆ and Ag/AgBr/MgBi₂O₆ composites exhibit diffraction peaks corresponding to both MgBi₂O₆ (m) and AgBr (a), confirming the successful synthesis of the composite materials with crystal planes consistent with the literature standards. In addition, as shown in Figure 1, no other crystal phases can be detected, indicating that no impurities are formed.

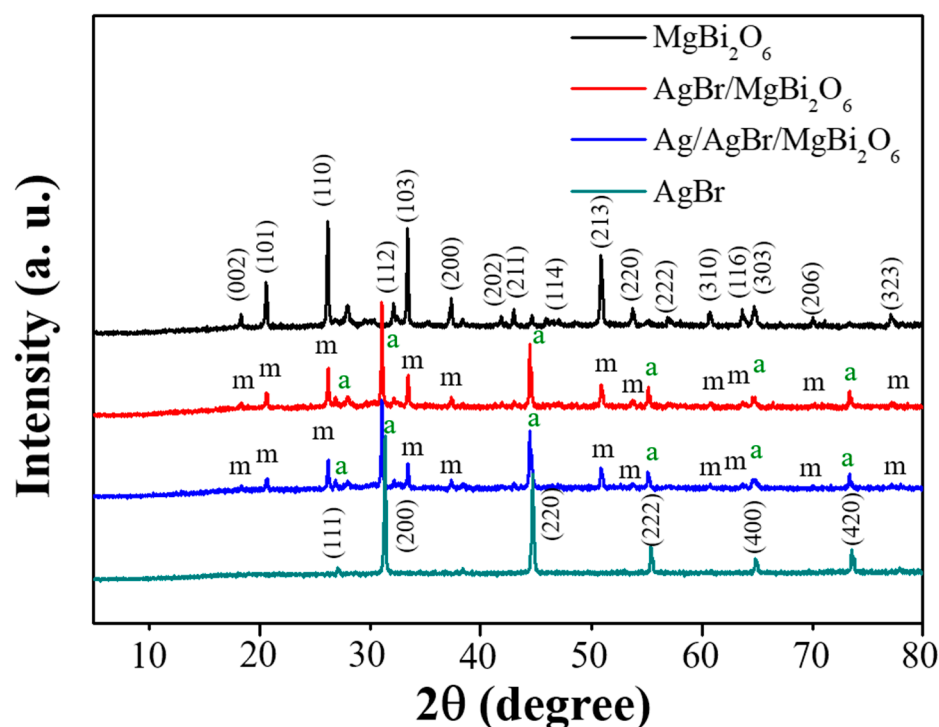


Figure 1. XRD spectra of MgBi₂O₆, AgBr/MgBi₂O₆, Ag/AgBr/MgBi₂O₆, and AgBr. A—AgBr, m—MgBi₂O₆.

As shown in Figure S1, the SEM images reveal that the morphology of MgBi₂O₆ consists of cuboidal structures with smooth surfaces, ranging in size from 50 nm to 600 nm, without any attached particles. Figure S2 presents the SEM of AgBr/MgBi₂O₆ synthesized

via the co-precipitation method, in which AgBr is deposited on the MgBi₂O₆ surface. Here, irregular spherical AgBr particles, with sizes between approximately 70 nm and 280 nm, are distributed across the cuboidal MgBi₂O₆ structures. Subsequently, Ag/AgBr/MgBi₂O₆ was synthesized through the photoreduction of AgNPs, as depicted in Figure S3. In this image, the cuboidal MgBi₂O₆ surface is scattered with irregularly shaped AgBr particles, which appear rough and granular at a higher magnification (50.0 K), with Ag ranging from 20 nm to 30 nm in size. EDS-mapping of the photocatalysts indicates a homogeneous distribution of elements throughout each material.

As shown in Figure 2A, MgBi₂O₆ displays a square morphology with an average size of approximately 55 nm. This observation is consistent with SEM analysis, which reveals lattice spacing of 0.3410 nm, 0.2794 nm, and 0.5375 nm, corresponding to the MgBi₂O₆ crystal planes (110), (112), and (103), respectively. Figure 2B illustrates AgBr/MgBi₂O₆ with a morphology similar to that observed in SEM. The AgBr/MgBi₂O₆ particle size is around 300 nm, while AgBr measures approximately 85 nm. The lattice spacing of MgBi₂O₆ and AgBr are 0.2414 nm and 0.2890 nm, corresponding to the (200) crystal planes of MgBi₂O₆ and AgBr, respectively. Figure 2C presents Ag/AgBr/MgBi₂O₆, consistent with the SEM observations, where AgBr is attached to the MgBi₂O₆ surface, and AgBr's surface appears rough due to the presence of photoreduced AgNPs of smaller size. At the crystal interface, the lattice spacing of 0.4327 nm and 0.2042 nm are observed, corresponding to the MgBi₂O₆ (101) and AgBr (220) crystal planes, respectively.

Figure 3A shows the UV-Vis DRS of the photocatalyst materials synthesized in this study. The absorption edges, determined by extrapolating the tangent lines to the *x*-axis, are located at 837 nm, 810 nm, 963 nm, 1029 nm, and 494 nm, corresponding to MgBi₂O₆, AgBr/MgBi₂O₆, Ag/AgBr/MgBi₂O₆, and AgBr, respectively. The band gaps (*E_g*) of these semiconductors were calculated using the Kubelka-Munk function and *Tauc* plots, where *hν* versus (*Ahν*)² allows for estimating *E_g* from the *x*-axis intercept [22,47,48]. The resulting band gaps for MgBi₂O₆, AgBr/MgBi₂O₆, Ag/AgBr/MgBi₂O₆, and AgBr are 1.66 eV, 1.72 eV, 1.45 eV, and 2.60 eV, respectively (Table 1). *E_g* significantly impacts photocatalytic efficiency and practical applications: materials with higher *E_g* value predominantly absorb ultraviolet light, which constitutes only ~5% of the solar spectrum, thereby limiting their effectiveness under visible light for solar-driven photocatalysis. Conversely, materials with lower *E_g* values can absorb visible light, improving their performance in solar-driven applications such as pollutant degradation and environmental remediation. Furthermore, the band edge positions of MgBi₂O₆ and AgBr can be calculated using the following empirical formula:

$$E_{VB} = \chi - E_e + 0.5E_g$$

$$E_{CB} = E_{VB} - E_g$$

where *E_{VB}* and *E_{CB}* are the valance band (VB) edge potential and conduction band (CB) edge potential. *χ* is the absolute electronegativity, and *E_e* is the potential energy of a free electron in a standard hydrogen electrode (4.5 eV) [44]. The values of *χ* for MgBi₂O₆ and AgBr are 6.11 and 5.81 eV, respectively. Based on the *E_g* of MgBi₂O₆ (1.66 eV) and AgBr (2.60 eV), the values of *E_{CB}* and *E_{VB}* for MgBi₂O₆ are calculated to be 0.78 and 2.44 eV, and those for AgBr are 0.01 and 2.61 eV, respectively.

Table 1. *E_g*, CB, and VB of MgBi₂O₆, AgBr/MgBi₂O₆, Ag/AgBr/MgBi₂O₆, Ag/MgBi₂O₆, and AgBr.

Series	<i>E_g</i> (eV)	CB (eV)	VB (eV)
MgBi ₂ O ₆	1.66	0.78	2.44
AgBr/MgBi ₂ O ₆	1.72	-	-
Ag/AgBr/MgBi ₂ O ₆	1.45	-	-
AgBr	2.60	0.01	2.61

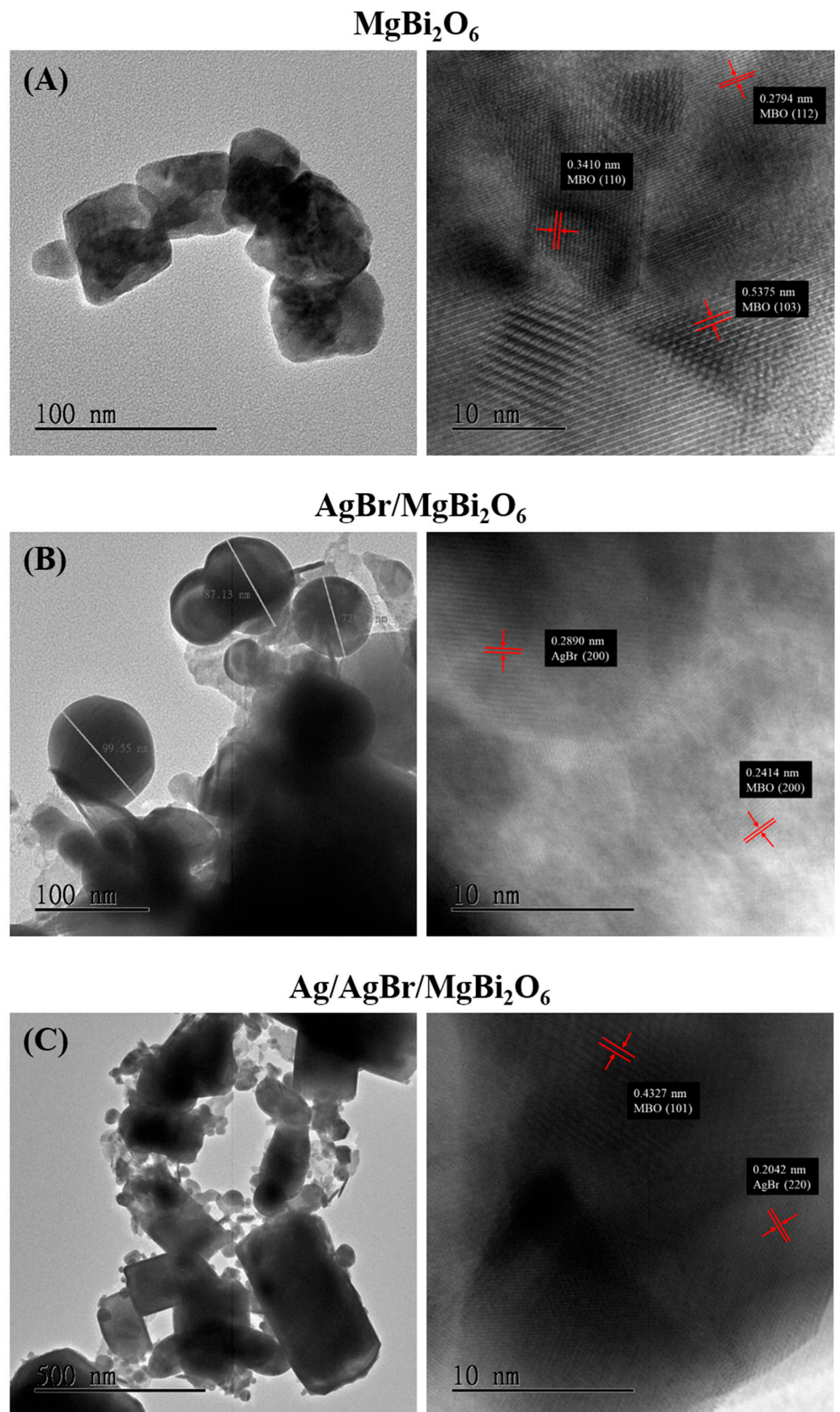


Figure 2. TEM images of (A) MgBi₂O₆, (B) AgBr/MgBi₂O₆, and (C) Ag/AgBr/MgBi₂O₆ composites.

As shown in Figure 2A, the absorption edge of AgBr at 494 nm falls within the visible light spectrum, indicating that surface modification of AgBr enhances light absorption in this range. Additionally, Figure 2B demonstrates that the E_g of Ag/AgBr/MgBi₂O₆ is reduced following photoreduction, which lowers the energy barrier for electron transition from the valence to the conduction band and facilitates electron-hole separation.

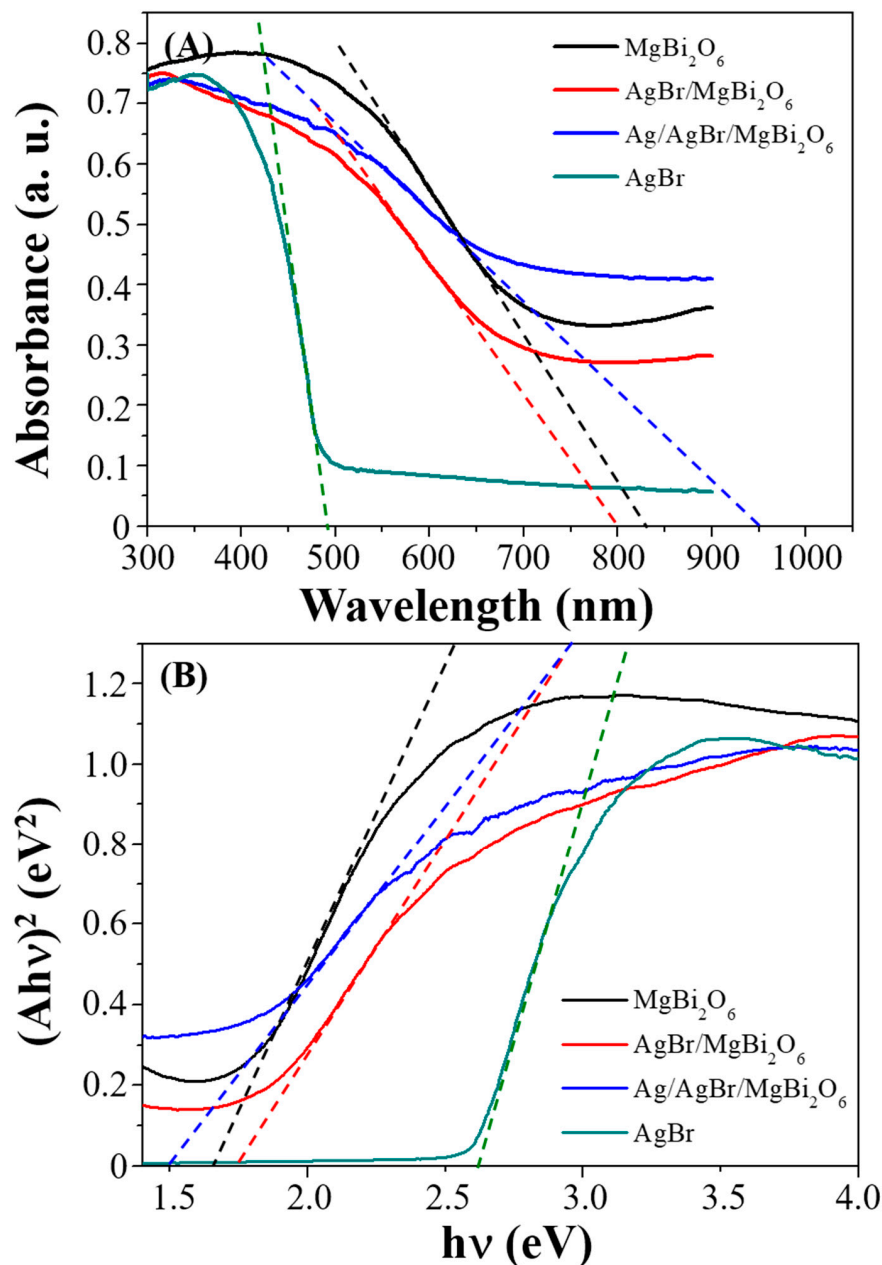


Figure 3. (A) UV-Vis DRS spectra and (B) the corresponding $(Ah\nu)^2$ versus $h\nu$ curves of MgBi₂O₆, AgBr/MgBi₂O₆, Ag/AgBr/MgBi₂O₆, and AgBr.

In this study, the synthesized catalysts were analyzed using an XPS spectrometer to investigate the chemical composition and surface electronic states of the prepared samples. The XPS spectrum of MgBi₂O₆, shown in Figure S4, reveals that the sample comprises oxygen, bismuth, and magnesium with atomic ratios of 60.1%, 24.4%, and 15.5%, respectively. The high-resolution spectrum indicates a peak at 1303.2 eV, corresponding to the Mg 1s level of Mg(II). After peak deconvolution, the binding energies of 49.57 eV and 48.35 eV are assigned to Mg(II) and Mg, respectively, with Mg(II) representing approximately 69.3% of

the total Mg content. In the high-resolution Bi spectrum, two distinct peaks at 163.8 eV and 163.3 eV correspond to Bi 4f_{5/2}, while peaks at 158.6 eV and 158.0 eV correspond to Bi 4f_{7/2}, indicative of Bi(V) and Bi(III) states [49,50]. The high-resolution O spectrum shows peaks at 531.1 eV, 530.7 eV, and 529.0 eV, attributed to O, O⁻, and O²⁻, respectively.

The XPS spectrum of AgBr/MgBi₂O₆ is presented in Figure S5, showing that the sample comprises O, Bi, Ag, Mg, and Br with atomic proportions of 55.8%, 20.7%, 10.7%, 6.8%, and 6.1%, respectively. In the high-resolution XPS spectrum of Ag, two main peaks are observed for Ag 3d_{3/2} and Ag 3d_{5/2}. Deconvolution of these peaks reveals binding energies at 373.4 eV and 367.4 eV for Ag(I) and at 373.1 eV and 367.2 eV for metallic Ag, with Ag(I) being the predominant form. The high-resolution Br spectrum displays peaks at 68.68 eV and 67.65 eV, corresponding to Br 3d_{3/2} and Br 3d_{5/2}, respectively. The Mg XPS spectrum shows a peak at 1303.2 eV, attributed to the Mg 1s orbital of Mg(II), consistent with the spectrum in Figure S4. Further deconvolution identifies peaks at 49.59 eV and 48.65 eV, corresponding to Mg(II) and metallic Mg, respectively. In the high-resolution Bi spectrum, Bi 4f_{5/2} and Bi 4f_{7/2} peaks are split into four peaks, with 163.7 eV and 158.5 eV assigned to Bi(V) and 163.5 eV and 158.1 eV to Bi(III) [49,50]. For oxygen, the high-resolution XPS reveals peaks at 531.1 eV, 530.8 eV, and 529.1 eV, corresponding to O, O⁻, and O²⁻, with O²⁻ being the dominant form at approximately 44.3% [51].

The XPS spectrum of Ag/AgBr/MgBi₂O₆ is presented in Figure S6, showing that the sample contains O, Ag, Bi, Br, and Mg, with atomic proportions of 44.4%, 22.4%, 15.4%, 12.1%, and 5.7%, respectively. After photo-reduction, the increased silver content confirms the successful formation of silver nanoparticles on the surface. Consequently, the atomic ratio of Ag to Br in Ag/AgBr/MgBi₂O₆ rose to 1.85 compared to AgBr/MgBi₂O₆ (the atomic ratio of Ag to Br is 1.67). The high-resolution XPS spectrum of Ag displays characteristic peaks at Ag 3d_{3/2} and Ag 3d_{5/2}. After peak deconvolution, four distinct peaks are observed, with binding energies of 373.7 eV and 368.0 eV corresponding to Ag(I), and 373.6 eV and 367.6 eV corresponding to metallic Ag. The high-resolution Br spectrum shows peaks at 69.18 eV and 68.12 eV, attributed to Br 3d_{3/2} and Br 3d_{5/2}, respectively. For Mg, high-resolution XPS peaks at 49.6 eV and 48.0 eV correspond to Mg(II) and Mg, with Mg(II) accounting for approximately 56.4% of the Mg present. In the Bi spectrum, the Bi 4f_{5/2} and Bi 4f_{7/2} peaks are split into four peaks: 164.0 eV and 158.7 eV for Bi(V), the predominant oxidation state, and 163.5 eV and 158.3 eV for Bi(III) [49,50]. The high-resolution O spectrum shows peaks at 532.1 eV, 530.8 eV, and 529.3 eV, corresponding to O, O⁻, and O²⁻, with O²⁻ as the dominant form at approximately 42.7% [51].

The resulting binding energies for the prepared MgBi₂O₆, AgBr/MgBi₂O₆, and Ag/AgBr/MgBi₂O₆ are also close to the previously reported values [22,44,52,53].

3.2. Degradation Performance

Prior to evaluating photocatalytic degradation, the optimized preparation conditions for Ag/AgBr/MgBi₂O₆, including the precursor mixing process (ultrasound or cell disruption), the light source used during photo-degrading MB (UV or white-light LED), the weight ratios of AgNO₃ to AgBr/MgBi₂O₆, and the photo-reduction reaction time, were systematically examined. Detailed results and discussions of these optimization factors are provided in the Supplementary Information (Figure S7).

The Ag/AgBr/MgBi₂O₆ synthesized under optimized conditions effectively degraded 15 ppm of MB. UV-Vis spectra of MB solutions at different times are illustrated in Figure 4B. The maximum absorption peak of MB is observed at 665 nm, with absorbance values progressively decreasing over the degradation period. Literature suggests that the degradation process involves two primary mechanisms: decolorization and mineralization [54,55]. Decolorization refers to the breakdown of chromophores and the fragmentation of organic molecules into smaller ones, often resulting in peak shifts or the appearance of new peaks. In contrast, mineralization directly converts organic molecules into CO₂ and H₂O, maintaining the same peak wavelength without new peak formation. Based on the results in Figure 4B, Ag/AgBr/MgBi₂O₆ was utilized for the degradation of MB. During the first

30 min of illumination (indicated by the black dashed line), mineralization was identified as the predominant degradation mechanism. After 30 min, a shift in the maximum absorption peak (red dashed line) was observed, indicating a transition toward decolorization. These spectral changes align with the gradual alteration in dye color over time, as illustrated in Figure 4A.

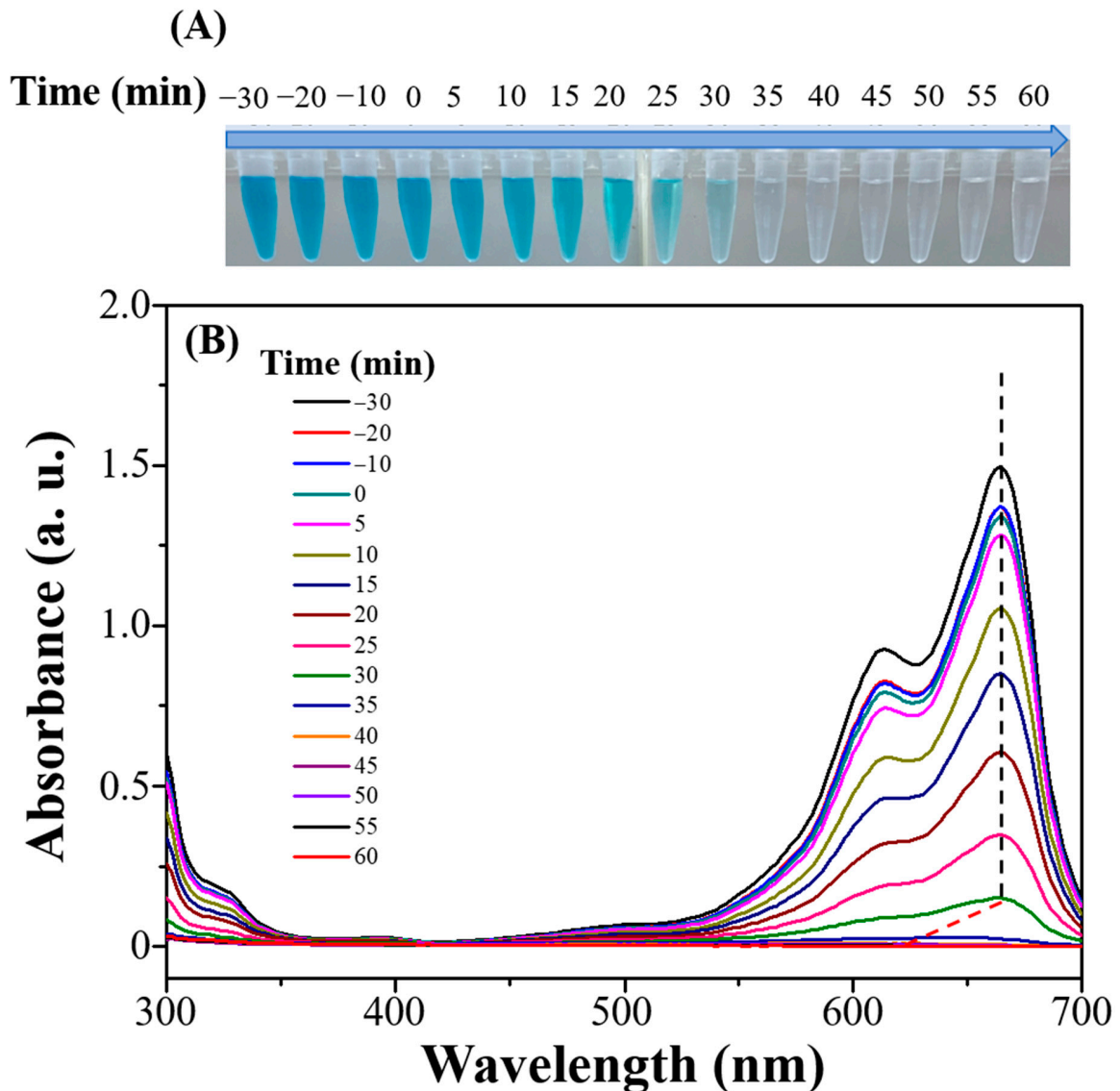


Figure 4. (A) Photograph images and (B) UV-Vis spectra of MB solutions under visible light irradiation using Ag/AgBr/MgBi₂O₆ composites at different times.

The photocatalytic performance of the synthesized catalysts (MgBi₂O₆, AgBr/MgBi₂O₆, Ag/AgBr/MgBi₂O₆, and AgBr) was assessed for MB degradation under visible light irradiation. Figure 5A illustrates the changes in MB concentration (C/C_0) over irradiation time for each photocatalyst, where C_0 is the initial MB concentration, and C is the concentration at time t . MB demonstrates negligible degradation without a photocatalyst under visible light irradiation (We will present the results later). The results in Figure 5A reveal significant differences in MB degradation across the photocatalysts within a 120 min observation period, with Ag/AgBr/MgBi₂O₆ emerging as the most effective catalyst. In addition, based on the light-off adsorption experiments (30 min) shown in Figure 5A, the observed differences in saturation coverage highlight a potential increase in surface area or improved adsorption properties for AgBr/MgBi₂O₆ and Ag/AgBr/MgBi₂O₆ composites.

This approach could serve as a preliminary indicator of effective surface area changes for different catalysts. The kinetics of MB degradation were further analyzed (Figure 5B), indicating a pseudo-first-order reaction. From the data in Figure 5B, the pseudo-first-order rate constants (k) for MB degradation by MgBi_2O_6 , $\text{AgBr}/\text{MgBi}_2\text{O}_6$, $\text{Ag}/\text{AgBr}/\text{MgBi}_2\text{O}_6$, and AgBr were determined to be 0.0162, 0.0661, 0.1223, and 0.0102 min^{-1} , respectively. Notably, the rate constant for $\text{Ag}/\text{AgBr}/\text{MgBi}_2\text{O}_6$ is approximately 7.55 times greater than that of MgBi_2O_6 . The pseudo-first-order kinetic equation, rate constants, and correlation coefficients are summarized in Table 2.

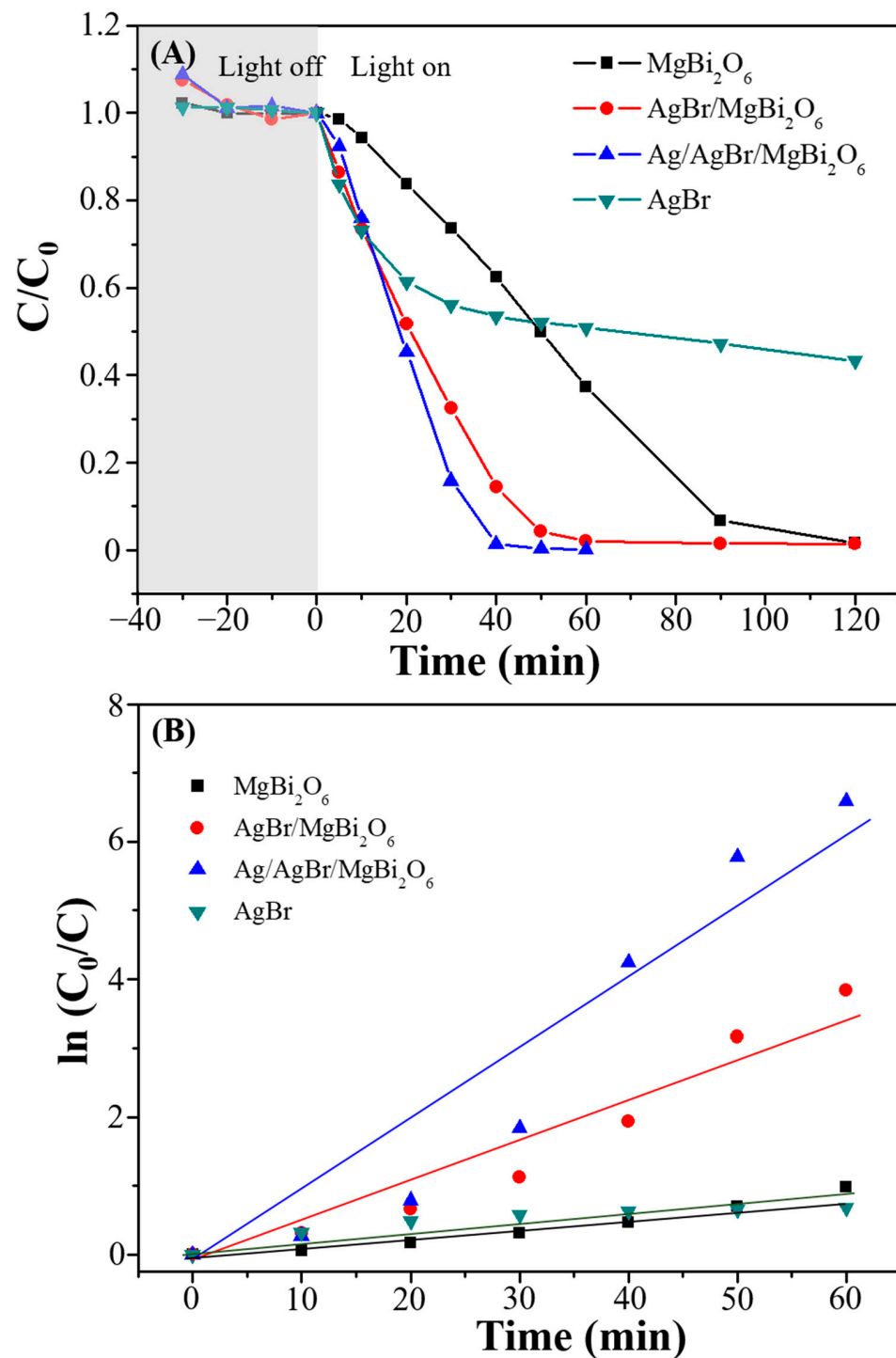


Figure 5. (A) Degradation performance of MB and (B) pseudo-first-order reaction for MB degradation by using MgBi_2O_6 , $\text{AgBr}/\text{MgBi}_2\text{O}_6$, and $\text{Ag}/\text{AgBr}/\text{MgBi}_2\text{O}_6$ composites.

Table 2. Kinetic parameters for the pseudo-first-order reaction equation of MgBi₂O₆, AgBr/MgBi₂O₆, Ag/AgBr/MgBi₂O₆, Ag/MgBi₂O₆, and AgBr.

Series	k (min ⁻¹)	Pseudo-First-Order Reaction	R ²
MgBi ₂ O ₆	0.0162	y = 0.0162x – 0.1002	0.9509
AgBr/MgBi ₂ O ₆	0.0661	y = 0.0661x – 0.4071	0.9473
Ag/AgBr/MgBi ₂ O ₆	0.1223	y = 0.1223x – 0.8789	0.9405
AgBr	0.0102	y = 0.0102x + 0.1725	0.8068

3.3. Degradation Mechanism

The photocatalytic reaction depends on the effective separation of photogenerated electron-hole pairs. In the PL spectrum, emitted light results from electron transitions from higher to lower energy states, reflecting free electron recombination. Consequently, PL intensity is proportional to the likelihood of electron-hole pair recombination. To assess whether the synthesized photocatalyst tends to facilitate electron transition from the conduction to the valence band post-excitation, which would reduce its lifespan, we measured the PL intensity of the powder samples at an excitation wavelength of 325 nm and an emission wavelength of 400 nm, as shown in Figure 6A. Compared to MgBi₂O₆, the PL intensity of AgBr/MgBi₂O₆ and Ag/AgBr/MgBi₂O₆ was significantly lower, suggesting the formation of an n-type electron and p-type hole space charge region upon light excitation. Additionally, the internal electric field established at the p–n heterojunction enhances charge separation and accelerates charge transfer. The p–n heterojunction formation suppresses electron-hole recombination, thereby enhancing the photocatalytic efficiency. This demonstrates that p–n heterojunction materials such as AgBr/MgBi₂O₆ and Ag/AgBr/MgBi₂O₆ effectively limit electron-hole recombination, improving photocatalytic performance.

The prepared MgBi₂O₆, AgBr/MgBi₂O₆, and Ag/AgBr/MgBi₂O₆ photocatalysts were individually coated onto the surface of an ITO electrode to fabricate a custom photocurrent electrode, enabling measurement of current density (μA/cm²). The photocurrent measurement reflects the combined effects of photogenerated electron quantity and electron-hole separation efficiency. The highest photocurrent intensity observed in the heterojunction indicates an increased number of photogenerated electrons and efficient charge transfer, signifying a higher electron-hole pair separation efficiency. As shown in Figure 6B, the photocurrent response is reproducible over multiple cycles of visible light switching, confirming the synthesized photocatalyst's stability under illumination. Among the samples, Ag/AgBr/MgBi₂O₆ exhibited the highest current density, approximately 14 ± 2 μA/cm², followed by AgBr/MgBi₂O₆ (10 ± 0.2 μA/cm²) and MgBi₂O₆ (3.5 ± 0.5 μA/cm²). Notably, the photocurrent trends also correlate with degradation efficacy, reinforcing the impact of post-illumination current response on photocatalytic performance.

To investigate the charge transfer properties of the photocatalyst, EIS was employed. Equivalent circuit modeling, as shown in the inset of Figure 6C, identifies R_s as the internal resistance, C_{dl} as the electric double-layer capacitance, and R_{CT} as the charge transfer resistance. In the Nyquist plots, a smaller semicircle radius corresponds to a lower R_{CT} value, indicating enhanced charge transfer efficiency and more effective separation of photogenerated electron-hole pairs. The R_{CT} values for MgBi₂O₆, AgBr/MgBi₂O₆, and Ag/AgBr/MgBi₂O₆ are 47.20 Ω, 42.58 Ω, and 39.54 Ω, respectively. Among the photocatalysts, Ag/AgBr/MgBi₂O₆ exhibits the lowest R_{CT} value, reflecting the highest charge transfer efficiency. This also aligns with its narrower bandgap, facilitating effective electron-hole pair separation and thus improving photocatalytic performance.

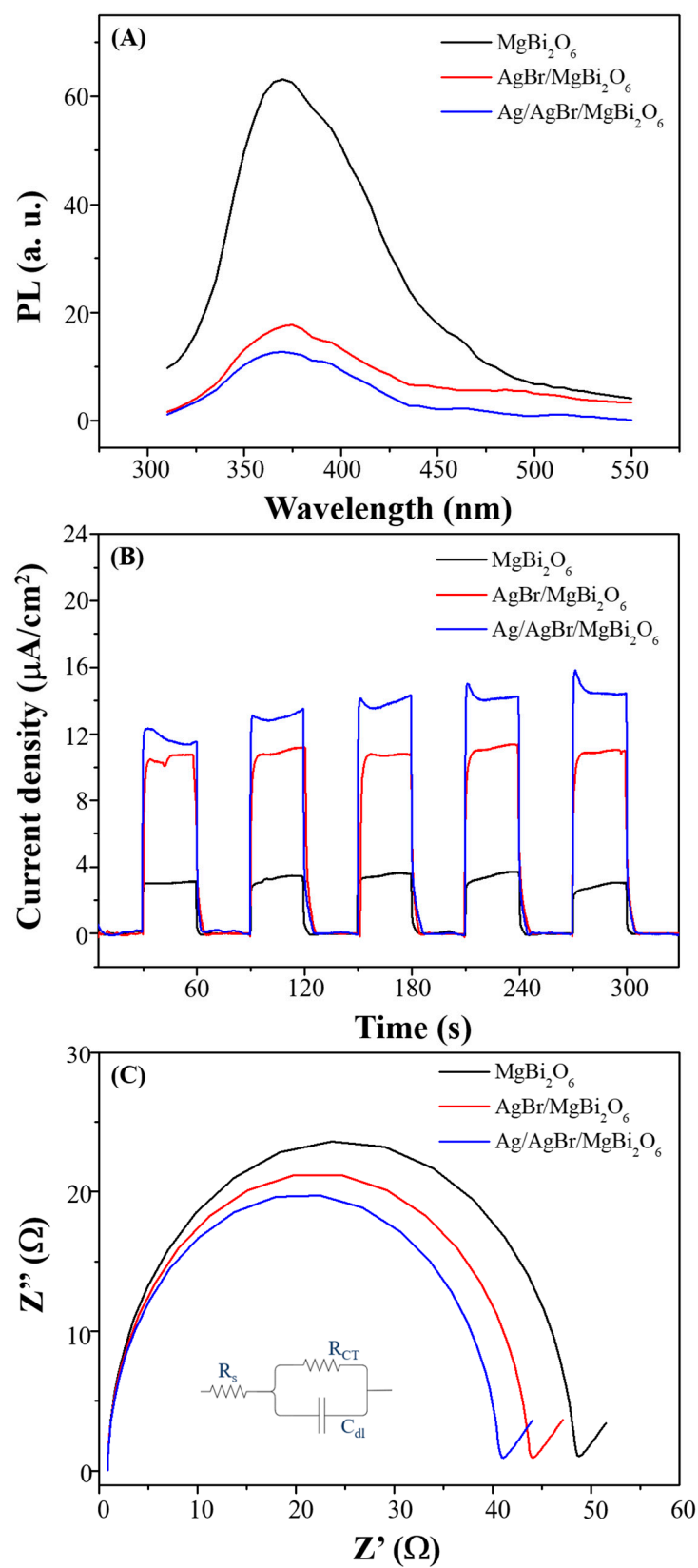


Figure 6. (A) PL, (B) Current density, and (C) EIS analysis of MgBi₂O₆, AgBr/MgBi₂O₆, and Ag/AgBr/MgBi₂O₆ composites.

To identify the main reactive species involved in the MB degradation process, a series of trapping experiments were conducted using specific scavengers. EDTA disodium salt

(1 mmol) was added to capture holes (h^+), while *t*-BuOH (1 mmol) was used to scavenge hydroxyl radicals ($\bullet OH$). Additionally, nitrogen gas was bubbled into the solution for 15 min before and continuously during the degradation experiment to remove dissolved oxygen, thereby inhibiting the formation of superoxide radicals ($\bullet O_2^-$). The effects of these scavengers on MB degradation were assessed by comparing the degradation efficiency in their presence to a control experiment without any scavenger. A significant reduction in MB degradation efficiency upon adding a scavenger indicates the involvement of the corresponding reactive species in the photocatalytic process. As shown in Figure 7, adding EDTA disodium salt reduced the MB degradation efficiency to 29.4% after 40 min, demonstrating that holes (h^+) are the main reactive species responsible for MB degradation by the Ag/AgBr/MgBi₂O₆ photocatalyst.

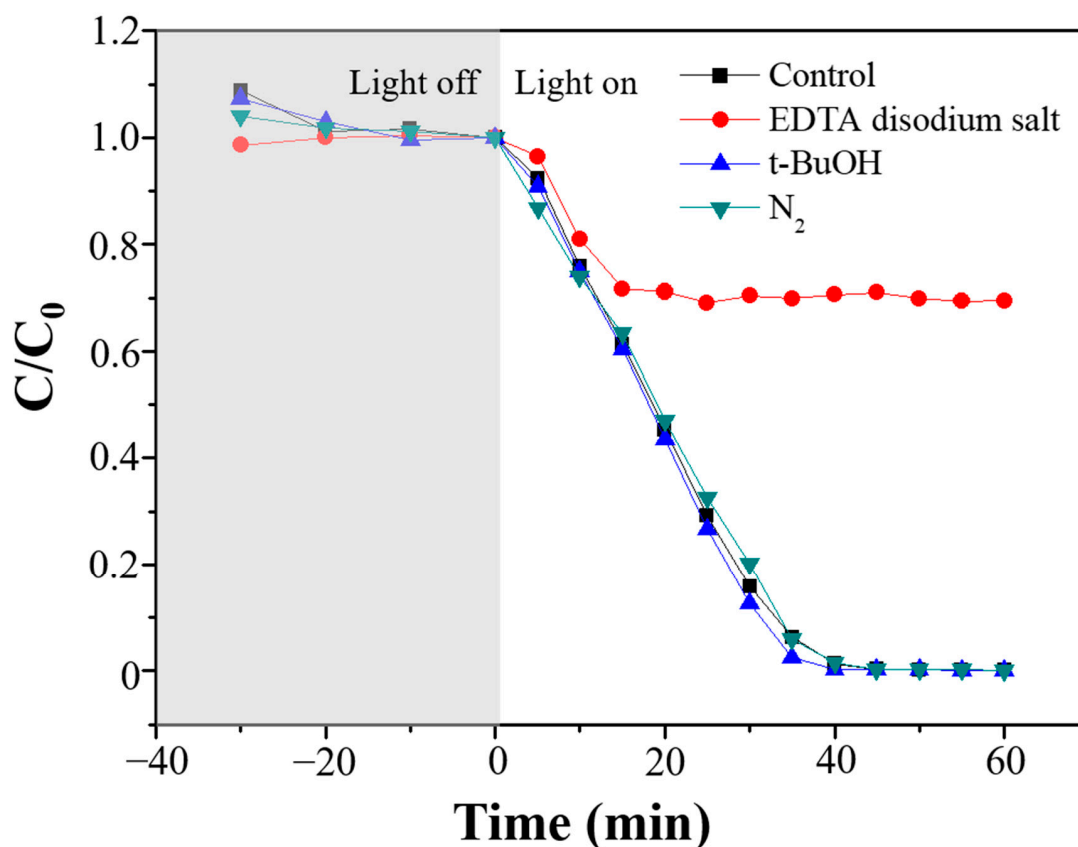
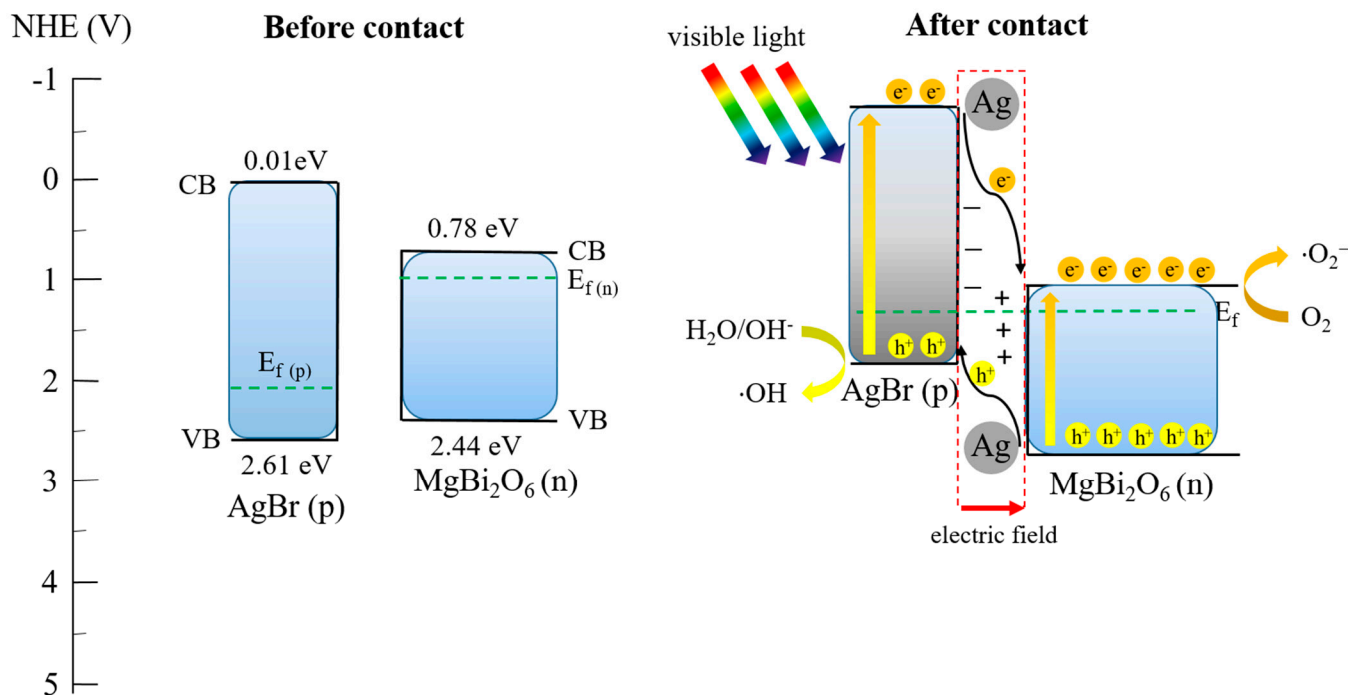


Figure 7. Scavenger tests of Ag/AgBr/MgBi₂O₆ composites.

Based on the above discussion, a proposed mechanism for the photocatalytic reaction is illustrated in Scheme 1. AgBr, a p-type semiconductor, and MgBi₂O₆, an n-type semiconductor, form a p–n heterojunction, establishing an internal electric field that accumulates negative charges on AgBr and positive charges on MgBi₂O₆ [22,44]. Under visible light excitation, AgBr strongly absorbs light energy, promoting electrons to its conduction band. These electrons are then transferred to AgNPs due to the internal electric field. Enhanced by the SPR effect of AgNPs, the electrons are further transferred to the conduction band of MgBi₂O₆, where they react with oxygen to form $\bullet O_2^-$ radicals. Simultaneously, holes in the valence band of MgBi₂O₆ migrate to the valence band of AgBr, generating $\bullet OH$ radicals upon reacting with water. This efficient electron and hole separation, enhanced by the SPR effect of AgNPs, significantly reduces electron-hole recombination. The generated electrons, holes, and reactive species, such as $\bullet O_2^-$ and $\bullet OH$, facilitate the degradation of MB through processes like ring opening, demethylation, and molecular decomposition. Alternatively, due to its high oxidation potential, MB can undergo direct redox reactions, yielding non-toxic byproducts, including CO₂ and H₂O.



Scheme 1. Possible mechanism of photodegradation using Ag/AgBr/MgBi₂O₆ composites.

3.4. Applications

As shown in Figure 8A, MB demonstrates negligible degradation without a photocatalyst. When compared with the commercially available photocatalyst P25, the degradation efficiency of MB reached only 1.8% after 40 min of reaction. Although P25 offers advantages such as high stability, various forms, and non-toxicity, its effectiveness is limited by its band gap (~3.2 eV), which restricts practical applications under visible light. In this study, the Ag/AgBr/MgBi₂O₆ photocatalyst was successfully synthesized, achieving effective electron-hole pair separation upon visible light excitation, leading to significant degradation efficiency.

A photocatalyst facilitates the photodegradation process by interacting with reactants during the reaction without being consumed, maintaining its mass and chemical properties unchanged. This study employs heterogeneous catalysis, which is advantageous due to its recyclability and alignment with principles of green chemistry and environmental sustainability for practical applications. Degradation tests were repeated after drying and reusing the material to assess the photocatalyst's reusability. As illustrated in Figure 8B, after three consecutive cycles, the photocatalyst demonstrated high degradation efficiency (1st used: 98.6%, 2nd used: 99.3%, and 3rd used: 99.1% within 40 min), indicating that Ag/AgBr/MgBi₂O₆ possesses excellent stability and ease of recovery in solution. Notably, an increase in dye adsorption over cycles suggests potential changes in the material's surface properties. Despite this, Ag/AgBr/MgBi₂O₆ consistently proved to be an effective and recyclable photocatalyst.

Total carbon (TC) encompasses both TOC and total inorganic carbon (TIC). When the visible color of degraded organic pollutants is fully removed, TOC analysis helps determine whether the process involves decolorization or complete mineralization. TOC measurement techniques include direct measurement and differential methods [56]. The direct measurement involves acidifying the sample and purging it with nitrogen to remove carbon dioxide from carbonate reactions, then measuring the remaining TOC. The differential method involves sequential injection into a high-temperature and a low-temperature furnace. The high-temperature furnace oxidizes all carbon (TC), while the low-temperature furnace measures only TIC. Subtracting TIC from TC yields the TOC value.

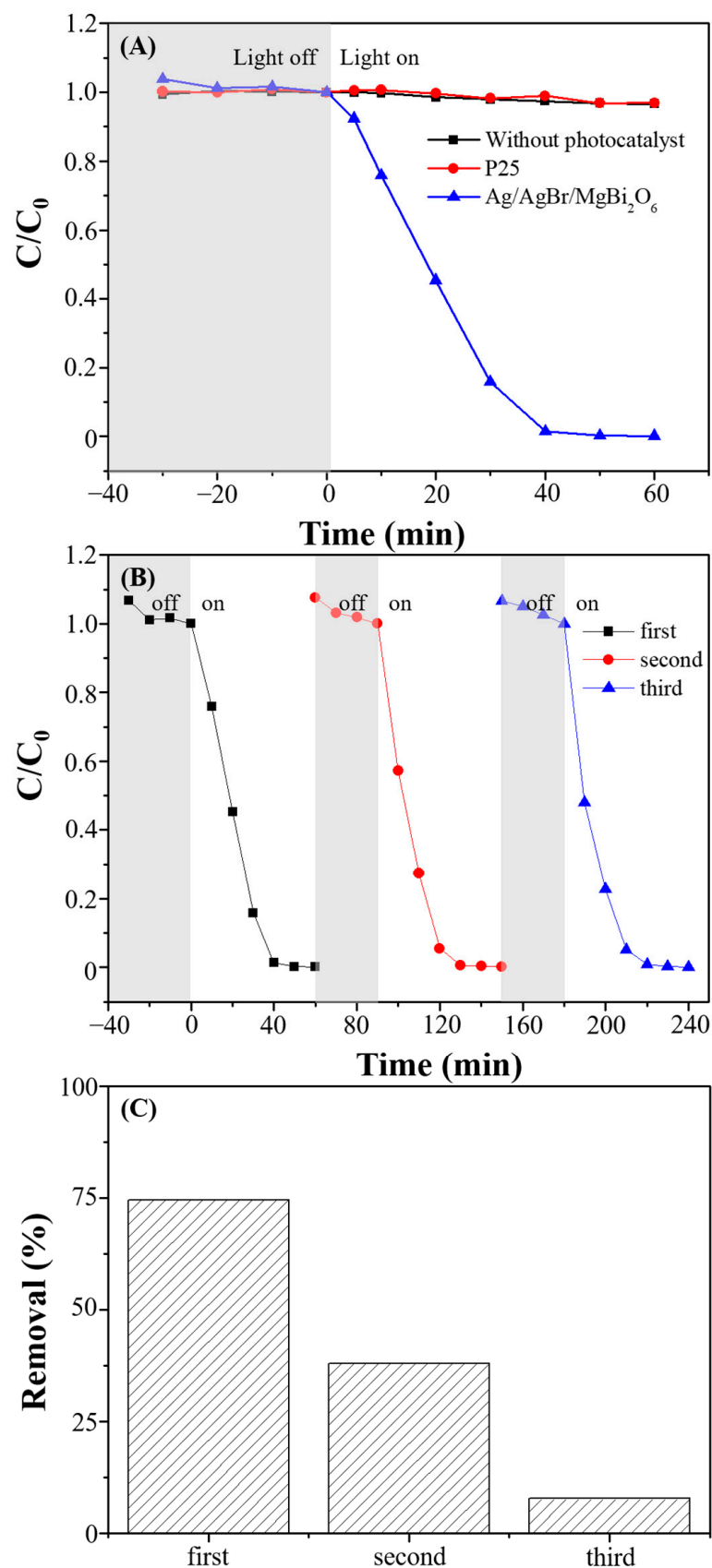


Figure 8. (A) Degradation performances of MB in the absence of catalyst and presence of P25 and Ag/AgBr/MgBi₂O₆ composites, (B) recycling used abilities, and (C) TOC experiments of Ag/AgBr/MgBi₂O₆ composites.

This experiment employed the direct measurement, wherein samples were acidified with phosphoric acid and purged with high-purity nitrogen. TOC was then measured following UV oxidation with peroxydisulfate and detected via infrared analysis. Using 15 ppm MB as the target pollutant, the TOC reduction after photodegradation is illustrated in Figure 8C, showing a 74.6% removal rate after the first use. This result confirms that full conversion of MB into CO₂ and H₂O was not achieved. This discrepancy arises because MB degradation involves a combination of pathways, including mineralization and partial breakdown into intermediate organic compounds (Figure 4B). Mineralization plays a significant role in the early stages, but the persistent intermediates limit complete TOC removal. In addition, the photocatalytic efficiency remained high across subsequent cycles, and the TOC exhibited significant reduction trends, likely indicating that decolorization dominated after the first used cycle. Moving forward, we will employ advanced analytical techniques such as liquid chromatography-mass spectrometry to identify and quantify the intermediates formed during MB degradation. This will provide a more comprehensive understanding of the photocatalytic mechanism and the nature of residual organic compounds.

In addition to MB, MR, MO, RhB, and R6G were selected as target dyes for degradation under identical experimental conditions. Each dye's peak absorbance was monitored per unit time, as illustrated in Figure 9A. The degradation efficiencies after 40 min were as follows: MR at 85.8%, MO at 90.1%, RhB at 99.9%, and R6G at 99.8%. While some dye was removed upon reaching adsorption-desorption equilibrium in dark conditions, indicating Ag/AgBr/MgBi₂O₆'s adsorption effect, the initial degradation might involve decolorization rather than full mineralization. RhB exhibited minimal adsorption issues, achieving a 96.7% degradation efficiency within just 20 min. These findings demonstrate that the Ag/AgBr/MgBi₂O₆ photocatalyst synthesized in this study shows strong catalytic activity for diverse dyes, as evidenced by the color changes of MR, MO, RhB, and R6G solutions, as shown in the top photograph of Figure 9A.

In real water samples, such as river and seawater, bacteria, heavy metals, minerals, and other substances can influence photodegradation reactions. To evaluate the material's feasibility in practical applications and assess whether these factors reduce the photocatalytic efficiency of Ag/AgBr/MgBi₂O₆, we compared real water samples with deionized water. The water samples included coastal seawater from Taichung City, Taiwan (Seawater 1), Changhua County, Taiwan (Seawater 2), river water from Tainan City, Taiwan (River Water 1), and from Taichung City, Taiwan (River Water 2). After pre-treatment, each sample was spiked with 15 ppm MB as the target pollutant. The degradation efficiency for each water source is shown in Figure 9B, reaching 96.0%, 92.6%, 87.2%, and 98.5% within 40 min, respectively. Notably, the degradation efficiency in Taichung River Water was closest to that observed in deionized water, while other samples exhibited strong dye adsorption. This difference may be attributed to mineral interference in seawater or the presence of porous substances that adsorb and decolorize the dye.

Table 3 compares the degradation performances using similar photocatalysts. The Ag/AgBr/MgBi₂O₆ photocatalyst, with its unique combination of AgNPs and AgBr with MgBi₂O₆, demonstrates significant promise for environmental remediation. Its ability to function efficiently under visible light conditions makes it suitable for real-world applications where UV light sources may not be practical. The high stability and reusability of the photocatalyst contribute to its economic viability, reducing the need for frequent replacement and minimizing environmental impact.

The innovative integration of AgNPs and AgBr with MgBi₂O₆ not only enhances the photocatalytic efficiency but also broadens the scope of photocatalytic applications. This material can potentially be applied to degrade a wide range of dyestuff, making it a versatile solution for pollution control. In summary, the Ag/AgBr/MgBi₂O₆ photocatalyst represents a significant advancement in photocatalysis, combining high efficiency, stability, and versatility. Its development paves the way for more effective and sustainable approaches to environmental cleanup and offers a robust platform for future research and innovation in photocatalytic materials.

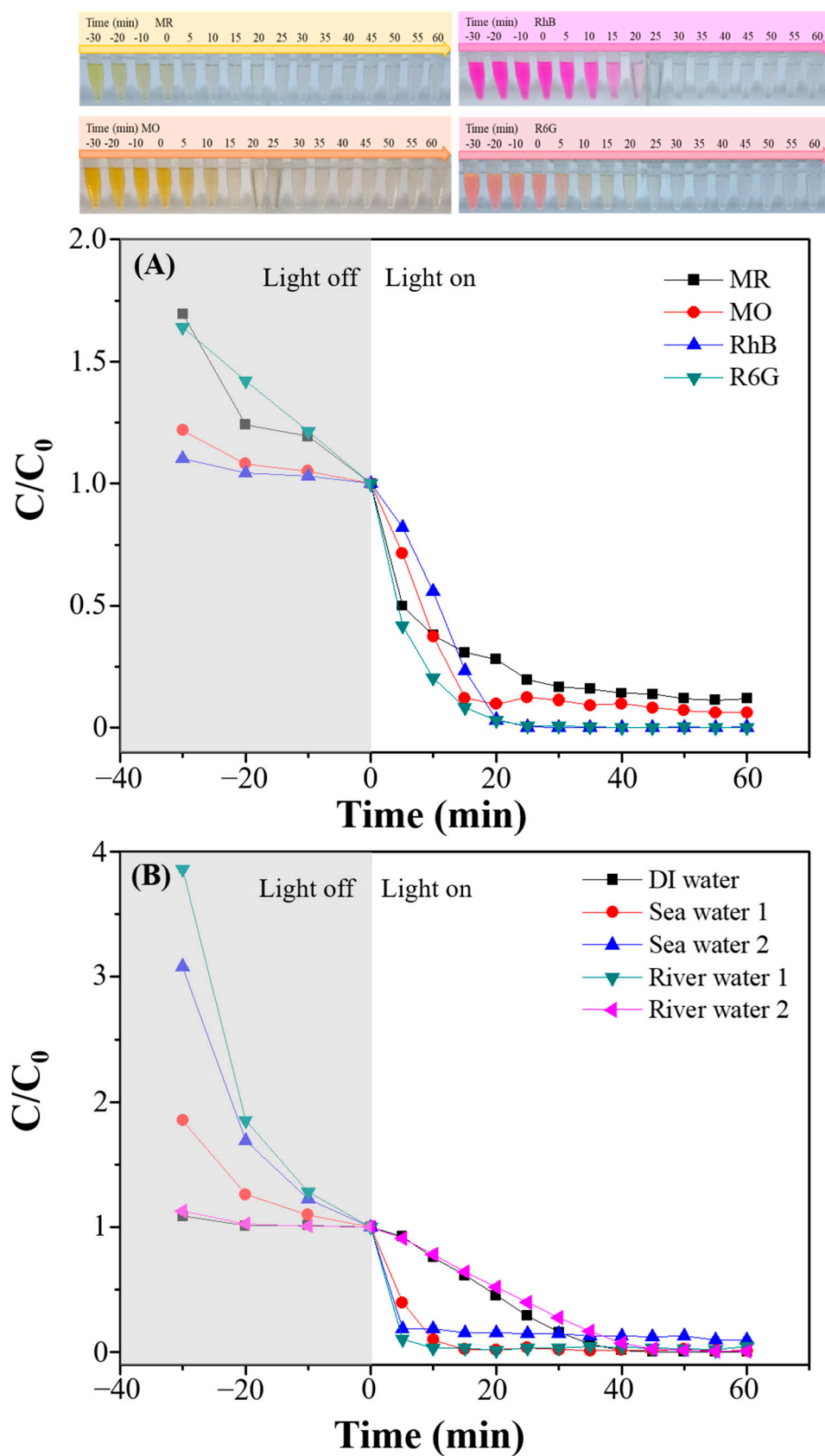


Figure 9. (A) Degradation performances of different dyestuff and photograph images of different dyestuff solutions, (B) degradation MB in the different environmental water samples using Ag/AgBr/MgBi₂O₆ composites.

Table 3. Comparisons of degradation performances using similar catalysts.

Series	Preparation	Degradation Performance	Real Samples	Ref.
AgBr/MgBi ₂ O ₆	Hydrothermal, coprecipitation	0.2 g catalyst/10 ppm MB/94% degradation in 35 min (300 W Xe lamp)	-	[44]
AgX/MgBi ₂ O ₆ (X = Cl, Br, I)	Co-precipitation	0.15 g catalyst/15 ppm MB/99.5% degradation in 20 min (2.5 W white-light LED irradiation)	-	[22]
Ag/MgBi ₂ O ₆	Heat treatment	0.2 g catalyst/10 ppm MB/98.6% degradation in 120 min (300 W Xe lamp)	-	[43]
AgBr-BiOBr	Co-precipitation	0.1 g catalyst/20 ppm RhB/80% degradation in 10 min (300 W Xe lamp)	-	[57]
AgBr-Ag-BiOBr	Precipitation	15 mg catalyst/15 ppm RhB/97% degradation in 20 min (300 W Hg lamp)	-	[58]
Ag-AgBr/ZnWO ₄	Hydrothermal, precipitation, sonication Microwave-assisted	2 g catalyst/50 ppm AR18/91% degradation in 60 min (500 W Xe lamp)	-	[27]
Ag/AgBr/Bi ₂ CrO ₆	hydrothermal, in-situ precipitation, photo-reduction method	0.1 g catalyst/10 ppm RhB/98.0% degradation in 30 min (250 W Xe lamp)	-	[34]
Ag/AgBr/MgBi ₂ O ₆	Hydrothermal, co-precipitation, photo-reduction	0.15 g catalyst/15 ppm MB/98.6% degradation in 40 min (2.5 W white-light LED irradiation)	Sea and river water	This study

The potential toxicity of the photocatalyst was not explicitly assessed in this study. However, previous research on similar photocatalysts has demonstrated that toxicity is largely dependent on the leaching of heavy metals or reactive intermediates during the photocatalytic process. To mitigate such concerns, the materials used in this study, such as MgBi₂O₆, AgBr, and Ag nanoparticles, were designed to be stable under photocatalytic conditions. Leaching studies could be conducted in future work to ensure minimal release of harmful ions, such as Ag⁺, into treated water. In future investigations, cytotoxicity assays or environmental toxicity assessments, such as testing on aquatic organisms or evaluating the photocatalyst's impact on microbial communities, will be performed to comprehensively evaluate its safety for environmental applications.

4. Conclusions

This study successfully developed a novel MgBi₂O₆ photocatalyst modified with AgBr and AgNPs through hydrothermal synthesis, co-precipitation, and photo-reduction methods. The Ag/AgBr/MgBi₂O₆ composite exhibited remarkable photocatalytic performance, achieving 98.6% degradation of MB within 40 min under 2.5 W white-light LED irradiation. This efficiency far surpassed the performance of MgBi₂O₆ and AgBr/MgBi₂O₆, underscoring the superior activity of the composite. The enhanced performance of Ag/AgBr/MgBi₂O₆ is attributed to its Z-scheme photocatalytic mechanism, which facilitates efficient electron-hole separation and minimizes recombination losses. The formation of a p-n heterojunction between AgBr and MgBi₂O₆ generates an internal electric field, enabling directional charge transfer and exclusive pathways for photogenerated carriers. Additionally, the SPR effect of Ag nanoparticles significantly boosts visible light absorption, further enhancing photocatalytic activity. The composite demonstrated excellent stability and reusability, retaining its degradation efficiency over multiple cycles. Its capability to degrade various dyes and in real water samples highlights its versatility and potential for real-world environmental remediation applications. These findings position Ag/AgBr/MgBi₂O₆ as a promising candidate for sustainable pollutant degradation under visible light irradiation.

Supplementary Materials: The following supporting information can be downloaded at: <https://www.mdpi.com/article/10.3390/nano14231865/s1>, Experiment section: synthesis of MgBi₂O₆, AgBr/MgBi₂O₆, and Ag/AgBr/MgBi₂O₆ under different conditions. Results and discussion: Optimum conditions for the synthesis of Ag/AgBr/MgBi₂O₆. Figure S1: SEM/EDS-mapping of MgBi₂O₆;

Figure S2: SEM/EDS-mapping of AgBr/MgBi₂O₆ composites; Figure S3: SEM/EDS-mapping of Ag/AgBr/MgBi₂O₆ composites; Figure S4: XPS analysis of MgBi₂O₆; Figure S5: XPS analysis of AgBr/MgBi₂O₆; Figure S6: XPS analysis of Ag/AgBr/MgBi₂O₆; Figure S7: Optimum conditions of Ag/AgBr/MgBi₂O₆ composites.

Author Contributions: Conceptualization, H.-Y.H. and M.K.A.; methodology, H.-Y.H. and M.K.A.; software, H.-Y.H. and M.K.A.; validation, H.-Y.H., M.K.A., S.T. and M.-Y.W.; formal analysis, H.-Y.H. and M.K.A.; investigation, H.-Y.H. and M.K.A.; resources, H.-Y.H. and M.K.A.; data curation, H.-Y.H. and M.K.A.; writing—original draft preparation, S.T. and M.-Y.W.; writing—review and editing, T.W. and Y.-W.L.; visualization, S.T., T.W. and Y.-W.L.; supervision, Y.-W.L.; project administration, Y.-W.L.; funding acquisition, Y.-W.L. All authors have read and agreed to the published version of the manuscript.

Funding: This research was funded by the Taiwan National Science and Technology Council (NSTC) under contracts (113-2113-M-018-001) and the Ministry of Education for the Taiwan Experience Education Program (TEEP).

Data Availability Statement: Data is contained within the article.

Conflicts of Interest: The authors declare no conflicts of interest.

References

1. Wani, N.A.; Malik, N.A.; Tantary, Y.R.; Jan, I.; Ahmad, T.; Wani, M.S. Emerging techniques for treatment of wastewater. In *Aquatic Contamination: Tolerance and Bioremediation*; John Wiley & Sons Ltd.: Hoboken, NJ, USA, 2024; pp. 1–23.
2. Ethiraj, S.; Samuel, M.S.; Indumathi, S. A comprehensive review of the challenges and opportunities in microalgae-based wastewater treatment for eliminating organic, inorganic, and emerging pollutants. *Biocatal. Agric. Biotechnol.* **2024**, *60*, 103316. [[CrossRef](#)]
3. Kulabhusan, P.K.; Campbell, K. Physio-chemical treatments for the removal of cyanotoxins from drinking water: Current challenges and future trends. *Sci. Total Environ.* **2024**, *917*, 170078. [[CrossRef](#)]
4. Wang, H.; Gao, X.; Zuo, Y. Research and application of water treatment technologies for emerging contaminants (ECs): A pathway to solving water environment challenges. *Water* **2024**, *16*, 1837. [[CrossRef](#)]
5. Obi, L.U.; Olisaka, F.N.; Onyia, F.C.; Innocent, I.H.; Onyemaechi, P. Physical and biological removal of the mass load of emergent pollutants from waste treatment facilities. In *Emergent Pollutants in Freshwater Plankton Communities*; CRC Press: Boca Raton, FL, USA, 2024; pp. 121–147.
6. Foo, W.H.; Chia, W.Y.; Ende, S.; Chia, S.R.; Chew, K.W. Nanomaterials in aquaculture disinfection, water quality monitoring, and wastewater remediation. *J. Environ. Chem. Eng.* **2024**, *12*, 113947.
7. Ma, J.; Chen, Y.; Zhou, G.; Ge, H.; Liu, H. Recent advances in photocatalytic degradation of tetracycline antibiotics. *Catalysts* **2024**, *14*, 762. [[CrossRef](#)]
8. García-López, E.I.; Aoun, N.; Marci, G. An overview of the sustainable depolymerization/degradation of polypropylene microplastics by advanced oxidation technologies. *Molecules* **2024**, *29*, 2816. [[CrossRef](#)] [[PubMed](#)]
9. Nikseresht, M.; Sohrabi, S.; Zhang, J.; Iranshahi, D.; Moraveji, M.K. Microfluidic platform for semiconductor and MOF integrated photocatalysts: A review over synthesis approaches and applications. *ChemistrySelect* **2024**, *9*, e202402249. [[CrossRef](#)]
10. Vaiano, V.; De Marco, I. Removal of azo dyes from wastewater through heterogeneous photocatalysis and supercritical water oxidation. *Separations* **2023**, *10*, 230. [[CrossRef](#)]
11. Villegas-Fuentes, A.; Rosillo-de la Torre, A.; Vilchis-Nestor, A.; Luque, P. Improvement of the optical, photocatalytic and antibacterial properties of ZnO semiconductor nanoparticles using different pepper aqueous extracts. *Chemosphere* **2023**, *339*, 139577. [[CrossRef](#)]
12. Hama Aziz, K.H.; Fatah, N.M.; Muhammad, K.T. Advancements in application of modified biochar as a green and low-cost adsorbent for wastewater remediation from organic dyes. *R. Soc. Open Sci.* **2024**, *11*, 232033. [[CrossRef](#)]
13. Ashkanani, Z.; Mohtar, R.; Al-Enezi, S.; Smith, P.K.; Calabrese, S.; Ma, X.; Abdullah, M. AI-assisted systematic review on remediation of contaminated soils with PAHs and heavy metals. *J. Hazard. Mater.* **2024**, *468*, 133813. [[CrossRef](#)] [[PubMed](#)]
14. Mohd, S.; Khan, A.M. Heterogeneous photocatalysis: Recent advances and applications. In *Sustainable Green Catalytic Processes*; Scrivener Publishing LLC: Beverly, MA, USA, 2024; pp. 141–163.
15. Mishra, K.; Devi, N.; Siwal, S.S.; Gupta, V.K.; Thakur, V.K. Hybrid semiconductor photocatalyst nanomaterials for energy and environmental applications: Fundamentals, designing, and prospects. *Adv. Sustain. Syst.* **2023**, *7*, 2300095. [[CrossRef](#)]
16. Wang, Y.; Sun, H.; Yang, Z.; Zhu, Y.; Xia, Y. Bismuth-based metal-organic frameworks and derivatives for photocatalytic applications in energy and environment: Advances and challenges. *Carbon Neutral.* **2024**, *3*, 737–767. [[CrossRef](#)]
17. Meira, A.C.R.; Tremarin, B.G.; Cursino, A.C.T.; de Oliveira Basso, R.L.; Bail, A.; Giona, R.M. In-situ preparation of a bismuth-based magnetic composite for catalytic reduction of 4-nitrophenol. *Mater. Chem. Phys.* **2022**, *277*, 125519. [[CrossRef](#)]
18. Palma Soto, E.; Rodriguez Gonzalez, C.A.; Luque Morales, P.A.; Reyes Blas, H.; Carrillo, A. Degradation of organic dye congo red by heterogeneous solar photocatalysis with Bi₂S₃, Bi₂S₃/TiO₂, and Bi₂S₃/ZnO thin films. *Catalysts* **2024**, *14*, 589. [[CrossRef](#)]

19. Li, B.; Liu, X.J.; Zhu, H.W.; Guan, H.P.; Guo, R.T. A review on Bi₂WO₆-based materials for photocatalytic CO₂ reduction. *Small* **2024**, *24*, 2406074. [[CrossRef](#)]
20. Sun, D.; Chen, Y.; Yu, X.; Yin, Y.; Tian, G. Novel defect-transit dual Z-scheme heterojunction: Sulfur-doped carbon nitride nanotubes loaded with bismuth oxide and bismuth sulfide for efficient photocatalytic amine oxidation. *J. Colloid Interface Sci.* **2024**, *674*, 225–237. [[CrossRef](#)]
21. Xia, P.; Song, Y.; Liu, Y.-Z.; Long, M.-X.; Yang, C.; Zhang, X.-Y.; Zhang, T. Advances in optical and electronic properties and applications of bismuth-based semiconductor materials. *J. Mater. Chem. C* **2024**, *12*, 1609–1624. [[CrossRef](#)]
22. Dai, Y.-D.; Lyu, R.-J.; Wu, T.; Huang, C.-C.; Lin, Y.-W. Influences of silver halides AgX (X= Cl, Br, and I) on magnesium bismuth oxide photocatalyst in methylene blue degradation under visible light irradiation. *J. Photochem. Photobiol. A-Chem.* **2020**, *397*, 112585. [[CrossRef](#)]
23. Adam, F.A.; Ghoniem, M.; Diawara, M.; Rahali, S.; Abdulkhair, B.Y.; Elamin, M.; Aissa, M.A.B.; Seydou, M. Enhanced adsorptive removal of indigo carmine dye by bismuth oxide doped MgO based adsorbents from aqueous solution: Equilibrium, kinetic and computational studies. *RSC Adv.* **2022**, *12*, 24786–24803. [[CrossRef](#)]
24. Chen, Q.; Gao, M.; Yu, M.; Zhang, T.; Wang, J.; Bi, J.; Dong, F. Efficient photo-degradation of antibiotics by waste eggshells derived AgBr-CaCO₃ heterostructure under visible light. *Sep. Purif. Technol.* **2023**, *314*, 123573. [[CrossRef](#)]
25. Liu, Q.; Li, X.; Wan, Z.; Xu, D.; Liu, C. Enhanced photocatalytic activity and antibacterial potential of a novel ternary ZnO-Ag₂MoO₄-AgI heterojunction photocatalyst. *Colloid Surf. A-Physicochem. Eng. Asp.* **2024**, *700*, 134765. [[CrossRef](#)]
26. Lee, P.-C.; Yang, Z.-R.; Kuo, C.-Y.; Shin, C.-H.; Lin, C.-B. Fabrication and characterization of visible-light-driven plasmonic photocatalyst Ag/AgCl/TiO₂ porous structure. *J. Mater. Eng. Perform.* **2023**, *32*, 7183–7194. [[CrossRef](#)]
27. Li, K.; Xue, J.; Zhang, Y.; Wei, H.; Liu, Y.; Dong, C. ZnWO₄ nanorods decorated with Ag/AgBr nanoparticles as highly efficient visible-light-responsive photocatalyst for dye AR18 photodegradation. *Appl. Surf. Sci.* **2014**, *320*, 1–9. [[CrossRef](#)]
28. Zhang, M.; Zhu, Y.; Li, W.; Wang, F.; Li, H.; Liu, X.; Zhang, W.; Ren, C. Double Z-scheme system of silver bromide@bismuth tungstate/tungsten trioxide ternary heterojunction with enhanced visible-light photocatalytic activity. *J. Colloid Interface Sci.* **2018**, *509*, 18–24. [[CrossRef](#)]
29. Yang, Y.; Guo, W.; Guo, Y.; Zhao, Y.; Yuan, X.; Guo, Y. Fabrication of Z-scheme plasmonic photocatalyst Ag@AgBr/g-C₃N₄ with enhanced visible-light photocatalytic activity. *J. Hazard. Mater.* **2014**, *271*, 150–159. [[CrossRef](#)]
30. Wang, Y.; Liu, H.; Wu, B.; Zhou, T.; Wang, J.; Zhou, J.; Li, S.; Cao, F.; Qin, G. Preparation and visible-light-driven photocatalytic property of AgX (X= Cl, Br, I) nanomaterials. *J. Alloys Compd.* **2019**, *776*, 948–953. [[CrossRef](#)]
31. Francis, M.M.; Thakur, A.; Balapure, A.; Dutta, J.R.; Ganesan, R. Fabricating effective heterojunction in metal-organic framework-derived self-cleanable and dark/visible-light dual mode antimicrobial CuO/AgX (X = Cl, Br, or I) nanocomposites. *Chem. Eng. J.* **2022**, *446*, 137363. [[CrossRef](#)]
32. Shi, H.; Li, G.; Sun, H.; An, T.; Zhao, H.; Wong, P.-K. Visible-light-driven photocatalytic inactivation of *E. coli* by Ag/AgX-CNTs (X= Cl, Br, I) plasmonic photocatalysts: Bacterial performance and deactivation mechanism. *Appl. Catal. B-Environ.* **2014**, *158*, 301–307. [[CrossRef](#)]
33. Zhang, W.; Zeng, X.; Lu, J.; Chen, H. Phase controlled synthesis and optical properties of ZnS thin films by pulsed laser deposition. *Mater. Res. Bull.* **2013**, *48*, 3843–3846. [[CrossRef](#)]
34. Ma, M.; Yan, X.; Mao, Y.; Kang, H.; Yan, Q.; Zhou, J.; Song, Z.; Zhu, H.; Li, Y.; Cui, L. All-solid-state Z-scheme AgBr/Bi₂CrO₆ heterostructure with metallic Ag as a charge transfer bridge for boosted charge transfer and photocatalytic performances. *Appl. Surf. Sci.* **2024**, *654*, 159471. [[CrossRef](#)]
35. Tian, L.; Li, J.; Wang, J.; Yang, Z.; Li, Y.; Zhang, L.; Zhang, G. Built-in electric field intensified by SPR effect to drive charge separation over Ag-AgI/Sb₂S₃ heterojunction for high-efficiency photocatalytic metronidazole mineralization. *Sep. Purif. Technol.* **2024**, *346*, 127443. [[CrossRef](#)]
36. Thennarasu, G.; Rajendran, S.; Kalairaj, A.; Rathore, H.S.; Panda, R.C.; Senthilvelan, T. A comprehensive review on the application of semiconductor nanometal oxides photocatalyst for the treatment of wastewater. In *Clean Technologies and Environmental Policy*; Springer: Berlin/Heidelberg, Germany, 2024; pp. 1–22.
37. Zhang, Y.; Liu, J.; Kang, Y.S.; Zhang, X.L. Silver based photocatalysts in emerging applications. *Nanoscale* **2022**, *14*, 11909–11922. [[CrossRef](#)]
38. Yao, Y.; Shen, Q.; Chen, Q.; He, Y.; Jiang, L.; Liu, J.; Li, Y.; Cao, X.; Yang, H. Ag/AgX (X = Cl, Br, or I) nanocomposite loaded on Ag₃PO₄ tetrapods as a photocatalyst for the degradation of contaminants. *ACS Appl. Nano Mater.* **2024**, *7*, 3711–3723. [[CrossRef](#)]
39. Azhar, M. Historical overview and future prospects of photocatalysis. In *Graphene-Based Photocatalysts: From Fundamentals to Applications*; Springer: Berlin/Heidelberg, Germany, 2024; pp. 47–65.
40. Nematov, D. Titanium dioxide and photocatalysis: A detailed overview of the synthesis, applications, challenges, advances and prospects for sustainable development. *J. Mod. Green Energy* **2024**, *3*, 1–34. [[CrossRef](#)]
41. Zhao, D.; Tang, X.; Liu, P.; Huang, Q.; Li, T.; Ju, L. Recent progress of ion-modified TiO₂ for enhanced photocatalytic hydrogen production. *Molecules* **2024**, *29*, 2347. [[CrossRef](#)]
42. Xu, F.; Hu, C.; Zhu, D.; Wang, D.; Zhong, Y.; Tang, C.; Zhou, H. One-step hydrothermal synthesis of nanostructured MgBi₂O₆/TiO₂ composites for enhanced hydrogen production. *Nanomaterials* **2022**, *12*, 1302. [[CrossRef](#)]
43. Zhong, L.; Hu, C.; Zhu, B.; Zhong, Y.; Zhou, H. *Synthesis and Photocatalytic Properties of MgBi₂O₆ with Ag Additions*; IOP Conference Series: Earth and Environmental Science; IOP Publishing: Bristol, UK, 2018; p. 022022.

44. Zhong, L.; Hu, C.; Zhuang, J.; Zhong, Y.; Wang, D.; Zhou, H. AgBr/MgBi₂O₆ heterostructured composites with highly efficient visible-light-driven photocatalytic activity. *J. Phys. Chem. Solids* **2018**, *117*, 94–100. [[CrossRef](#)]
45. Sanni, S.; Viljoen, E.; Ofomaja, A. Tailored synthesis of Ag/AgBr nanostructures coupled activated carbon with intimate interface interaction for enhanced photodegradation of tetracycline. *Process Saf. Environ. Protect.* **2021**, *146*, 20–34. [[CrossRef](#)]
46. Sanni, S.; Viljoen, E.; Ofomaja, A. Design of ordered Ag/AgBr nanostructures coupled activated carbon with enhanced charge carriers separation efficiency for photodegradation of tetracycline under visible light. *J. Mol. Liq.* **2020**, *299*, 112032. [[CrossRef](#)]
47. Liu, L.; Wang, D.; Zhong, Y.; Hu, C. Electronic, optical, mechanical and lattice dynamical properties of MgBi₂O₆: A first-principles study. *Appl. Sci.* **2019**, *9*, 1267. [[CrossRef](#)]
48. Mizoguchi, H.; Bhuvanesh, N.S.; Woodward, P.M. Optical and electrical properties of the wide gap, n-type semiconductors: ZnBi₂O₆ and MgBi₂O₆. *Chem. Com.* **2003**, 1084–1085. [[CrossRef](#)] [[PubMed](#)]
49. Ding, Y.; Zhang, G.; Wang, X.; Zhu, L.; Tang, H. Chemical and photocatalytic oxidative degradation of carbamazepine by using metastable Bi³⁺ self-doped NaBiO₃ nanosheets as a bifunctional material. *Appl. Catal. B-Environ.* **2017**, *202*, 528–538. [[CrossRef](#)]
50. Ding, Y.; Yang, F.; Zhu, L.; Wang, N.; Tang, H. Bi³⁺ self doped NaBiO₃ nanosheets: Facile controlled synthesis and enhanced visible light photocatalytic activity. *Appl. Catal. B-Environ.* **2015**, *164*, 151–158. [[CrossRef](#)]
51. Lamba, R.; Umar, A.; Mehta, S.K.; Anderson, W.A.; Kansal, S.K. Visible-light-driven photocatalytic properties of self assembled cauliflower-like AgCl/ZnO hierarchical nanostructures. *J. Mol. Catal. A Chem.* **2015**, *408*, 189–201. [[CrossRef](#)]
52. Hu, C.; Zhuang, J.; Zhong, L.; Zhong, Y.; Wang, D.; Zhou, H. Significantly enhanced photocatalytic activity of visible light responsive AgBr/Bi₂Sn₂O₇ heterostructured composites. *Appl. Surf. Sci.* **2017**, *426*, 1173–1181. [[CrossRef](#)]
53. Zhang, A.; Zhang, L.; Lu, H.; Chen, G.; Liu, Z.; Xiang, J.; Sun, L. Facile synthesis of ternary Ag/AgBr-Ag₂CO₃ hybrids with enhanced photocatalytic removal of elemental mercury driven by visible light. *J. Hazard. Mater.* **2016**, *314*, 78–87. [[CrossRef](#)]
54. Ali, S.; Ismail, P.M.; Khan, M.; Dang, A.; Ali, S.; Zada, A.; Raziq, F.; Khan, I.; Khan, M.S.; Ateeq, M. Charge transfer in TiO₂-based photocatalysis: Fundamental mechanisms to material strategies. *Nanoscale* **2024**, *16*, 4352–4377. [[CrossRef](#)]
55. Jabbar, Z.H.; Graimed, B.H.; Ammar, S.H.; Sabit, D.A.; Najim, A.A.; Radeef, A.Y.; Taher, A.G. The latest progress in the design and application of semiconductor photocatalysis systems for degradation of environmental pollutants in wastewater: Mechanism insight and theoretical calculations. *Mater. Sci. Semicond. Process* **2024**, *173*, 108153. [[CrossRef](#)]
56. Wojnárovits, L.; Homlok, R.; Kovács, K.; Tegze, A.; Takács, E. Wastewater characterization: Chemical oxygen demand or total organic carbon content measurement? *Molecules* **2024**, *29*, 405. [[CrossRef](#)] [[PubMed](#)]
57. Kong, L.; Jiang, Z.; Lai, H.H.; Nicholls, R.J.; Xiao, T.; Jones, M.O.; Edwards, P.P. Unusual reactivity of visible-light-responsive AgBr–BiOBr heterojunction photocatalysts. *J. Catal.* **2012**, *293*, 116–125. [[CrossRef](#)]
58. Liu, J.; Guo, H.; Zhang, L.; Yin, H.; Nie, Q. One-pot synthesis of AgBr-Ag-BiOBr nanosheets for efficient visible-light-driven photocatalysis. *Mater. Lett.* **2022**, *323*, 132556. [[CrossRef](#)]

Disclaimer/Publisher’s Note: The statements, opinions and data contained in all publications are solely those of the individual author(s) and contributor(s) and not of MDPI and/or the editor(s). MDPI and/or the editor(s) disclaim responsibility for any injury to people or property resulting from any ideas, methods, instructions or products referred to in the content.